https://doi.org/10.1016/j.scriptamat.2021.114117

Gradient nanotwinned CrCoNi medium-entropy alloy with strength-ductility synergy

Shuqing Yuan[a,1], Bin Gan[c,1], Lei Qian[a,1], Bo Wu[a], Hui Fu[a], Hong-Hui Wu[d], Chi Fai Cheung[a] and Xu-Sheng Yang[a,b*]

[a]*State Key Laboratory of Ultra-precision Machining Technology, Department of Industrial and Systems Engineering, The Hong Kong Polytechnic University, Hung Hom, Kowloon, Hong Kong, China (E-mail: xsyang@polyu.edu.hk)*

[b]*Hong Kong Polytechnic University Shenzhen Research Institute, Shenzhen, China*

[c]*Beijing Key Laboratory of Advanced High Temperature Materials, Central Iron and Steel Research Institute, Beijing, 100081, China*

[d]*School of Materials Science and Engineering, University of Science and Technology Beijing, Beijing 100083, China*

In this study, a high-strain rate ultra-precision machining technology named single point cubic boron nitride turning is developed to fabricate a gradient nanotwinned CrCoNi medium entropy alloy layer. The grain size of the ~ 150 μm-thick gradient layer is gradually refined from the original ~17 μm to ~25 nm in the topmost surface, exhibiting a significantly enhanced yield strength (from ~450 MPa to ~1100 MPa) and well-retained ductility of ~ 27%. High-resolution transmission electron microscope and atomistic simulations were mainly performed to unveil the size-dependent twinning mechanisms governing the gradient refinement process from the core to the topmost surface, i.e. transiting from the parallel twins segmenting ultrafine grains, twin-twin intersections refining rhombic blocks and rotating the intersected nanograins, and finally to the zero-macrostrain deformation nanotwinning in the refined nanograins. The machining process provides sufficient equivalent stress to activate the twinning partials for forming the gradient nanotwinned structure.

Keywords: Gradient nanotwinned structure; medium-entropy alloy; ultra-precision machining technology; high-resolution transmission electron microscope; twin-twin intersection.

[1] These authors contributed equally to this work.

[*] Corresponding author. xsyang@polyu.edu.hk (X.-S Yang). Tel: +852-27666604

Due to the severely suppressed multiplication and motion of dislocations by increased grain boundaries (GBs) [1], homogeneous nanograined (NG) metals (grain size below 100 nm) can significantly strengthen but largely downgrade the ductility [2]. Alternatively, the low-excess energy nano-sized twin boundary (TB) can not only effectively hinder dislocation motion, but also act as the stable interface for strengthening [3]. For instance, nanotwinned (NT) metals (e.g. nano-sized twins in submicron-sized ultrafine grains (UFGs)) show extraordinary strengthening with good ductility [4]. In addition, the strength-ductility dilemma can also be reconciled by constructing a unique gradient nanostructure (GNS), e.g. gradient distribution in phases, composition, and grain size/twin thickness [5-7], owing to the particular cooperative effects of strain/stress partitioning and strain gradient between different domains. GNS metals can be produced by various surface severe plastic deformation (SSPD) techniques, which generate the most severe plastic strain and strain rate in the topmost surface that gradually decrease toward the matrix region [8]. Noticeably, deformation twinning via partial dislocation slide would dominate the plasticity in low/medium-stacking fault energy (SFE) metals [9]. Along this line of thought, SSPD techniques are therefore highly expected to produce gradient nanotwinned (GNT) metals, which have concurrent gradients in grains and twins (i.e. small grains contain thin twins while large grains contain thick twins), thus achieving a superb strength-ductility combination. Extra strengthening and work hardening were reported in some low/medium-SFE GNT metals [10-12]. However, there is still limited literature concerned about the fabrication and mechanical properties of SSPD-produced GNT metals.

Medium/high-entropy alloys (M/HEAs) have drawn great attention due to their excellent properties [13]. Particularly, face-centered cubic (fcc) CrCoNi MEA with low SFE (22 ± 4 mJ/m^2) shows an impressive combination of strength and toughness/ductility, attributed to the strengthening mechanism mainly dominated by deformation twinning [14, 15]. Noticeably, “hard turning” technique was reported to achieve a gradient nanolaminate CrCoNi

MEA layer, in which the formed NTs and hexagonal close-packed (hcp) phase were evidenced to a high strain hardening capability [16]. Nevertheless, SSPD techniques still need to be further developed to produce the novel large-length scale GNT CrCoNi MEA with superior mechanical properties. Besides, the underlying twinning mechanisms governing the gradient refinement process should be unveiled by atomic observations of the microstructural evolution.

Increasing plastic strain rate at a given temperature can effectively facilitate the deformation twinning in low-SFE metals with large-length scale grain size [17]. Herein, a high-strain rate ultra-precision machining SSPD technique named single point cubic boron nitride turning (SPCBNT) has been developed to fabricate a GNT layer on CrCoNi MEA. Relative to some conventional machining technologies, the high-quality surface with nanometre-level surface roughness can be achieved in the workpiece processed by ultra-precision machining technology, in lieu of any additional post-polishing [18]. In addition, the ultra-precision machining process can impart a high strain rate (10^3-10^5 s^{-1}) in the topmost surface of the specimen. When adjusting the processing parameters (especially the rake angle is negative), it can be developed to effectively fabricate the GNS/GNT layer on the workpiece. As schematically shown in Fig. 1(a-b), ultra-precision SPCBNT process would lead to a pileup of material ahead of the tool, which thus “compress” back into the surface of the specimen with a high plastic strain rate, instead of the purely cutting [19]. Consequently, gradient strain rate and strain along the depth direction are generated to potentially promote the deformation twinning for generating large-length scale GNT CrCoNi MEA. Therefore, ultra-precision machining technology (including SPCBNT) can be considered as a cost-effective method for the fabrication of the ultra-precision/optics parts with enhanced mechanical properties for various engineering applications.

CrCoNi MEA specimen was produced first by vacuum induction melting using three high-purity equal-atomic elements (> 99.9 wt.%). Subsequently, the homogenization (1200 °C

for 6 hours), hot swaging (60% in reduction), and recrystallization (850 °C for 1 hour) processes were respectively conducted to obtain the homogeneous polycrystalline specimen [20]. Hence, cylindrical CrCoNi MEA specimen with a diameter of 10 mm and a length of 11 mm was prepared by wire-cutting for the SPCBNT process on a Moore Nanotech 450UPL machine (Moore precision tools Inc. USA). In detail, the spindle speed V_1, rake angle α', feed rate V_0, and cutting depth were respectively assigned as 500 rpm, −20° , 5 mm/min, and 10 μm in the SPCBNT process, which was repeated 20 passes. The cross-sectional images of the machined specimens were first checked by using an optical microscope (OM, Leica DMLM optical microscopy) and scanning electron microscope (SEM, TESCAN VEGA3), respectively, to verify the occurrence of the GNS layer. In addition, the variation of hardness along the depth direction from the surface to matrix was also determined by conducting the hardness testing on a Mitutoyo microhardness testing machine with loading force 0.5 kg for 15 s. Stress-strain curves of the original buck specimen and GNS layer with a gauge length of 4 mm and cross-section of 2 × 0.2 mm were obtained by carrying out the uniaxial tensile tests on an INSTRON 5565 material testing machine at the room temperature and strain rate of 5×10^{-4} s^{-1}. Plane-view high-resolution transmission electron microscope (HRTEM) observations at different depth layers were performed on a field emission JEM-2100F with an operating voltage of 200 kV to dissect the gradient refinement process governed by deformation twinning. For the plane-view TEM sample preparation at a certain depth layer, TEM slices were first mechanically polished to ~25 μm from the opposite side of the observed layer and then single-side ion thinned by the ion polishing system (Gatan 691).

In addition, molecular dynamics (MD) simulations were carried out to reveal the microstructural evolution during the SPCBNT process, especially the deformation twinning at the atomic level. LAMMPS code [21] and hybrid potentials (including the embedded-atoms method (EAM) potential [22], Morse potential and Tersoff potential [23]) were used to

construct a three-dimensional 30 × 60 × 45 nm CrCoNi MEA model, which includes 22 randomly oriented grains with an average grain size of 18 nm. Before the cutting process, the CrCoNi model was relaxed at room temperature and zero pressure for 200 ps to reach thermodynamic equilibrium using a NPT ensemble. As shown in Fig. 1(e), the workpiece was cut by the rigid tool with a rake angle of -45°, a cutting speed of 400 m/s and a cutting depth of 10 nm. In detail, the tool is placed on top of the workpiece and then moves down 10 nm, followed by right-to-left movement. A periodic boundary condition is maintained along the X-direction during machining.

OM image in Fig. 1(c) exhibits an obvious gradient plastic deformation zone with thickness of ~150 μm in the surface layer of CrCoNi MEA after the SPCBNT process. The refined NG zone in the surface area and high density of deformation twins in the subsurface region of the machined specimen are further displayed in the SEM picture in Fig. 1(d) and MD simulation results in Fig. 1(e). Accordingly, Fig. 1(f) gives the variation of hardness from the topmost surface to the matrix of the machined sample, together with the corresponding average grain size statistically determined based on the TEM characterizations. The averaged hardness in the topmost surface layer is ~ 410 HV, which gradually decreases to ~ 250 HV at the depth of ~ 150 μm and then unchanged onwards. Correspondingly, the average grain size gradually decreases from the original ~ 17 μm to ~ 25 nm in the topmost surface. The results consistently verify a ~ 150 μm-thick GNS layer on CrCoNi MEA produced by SPCBNT technology. The engineering tensile stress-strain curves of original and GNS specimens are shown in Fig. 1(g), which shows that the GNS layer possesses an obvious improvement in yield strength of ~ 1100 MPa, significantly higher than that of ~ 450 MPa of the original specimen. Meanwhile, a ductility of ~ 27% is well retained in the GNS layer. Fig. 1(h) clearly demonstrates the enhanced strength-ductility synergy of the GNS layer in comparison with other referenced CrCoNi MEAs which had comparable sample sizes and were tested at room temperature and close

strain rates.

A series of representative plane-view TEM images at different depths are given in Fig. 2 to present the microstructural evolution of the GNS layer on CrCoNi MEA experienced SPCBNT. In contrast to the original ~ 17 μm-size CGs at the ~200 μm-depth layer in Fig. 2(a), the sub-grains with the gain size of ~ 2 μm are formed at the depth of ~100 μm, as shown in Fig. 2(b) and small misorientations in the associated SAED in the inset. High-density dislocations can be found to accumulate at the GBs, attributing to form these sub-grains. With the increase of strain rate and strain, extensive parallel deformation twins with thickness of ~100 nm are initiated to segment the UFGs into twin lamellae, as TEM image at a depth of ~60 μm shown in Fig. 2(c). Furthermore, Fig. 2(d) and Fig. 2(e) show that lots of twin-twin intersections emerge at a depth of ~ 40 μm, so that UFGs are further refined into rhombic blocks with an average size of ~70 nm. When more approaching the machined top surface, NGs are formed. For example, Fig. 2(f-h) demonstrates that average grain sizes of NGs are gradually refined from ~ 60 nm at depth of ~ 20 μm to ~25 nm in the topmost surface. It should be noted that profuse nanograins containing deformation NTs always exist, as marked by red dash frames in Fig. 2(f-h). Accordingly, Fig. 2(i) statistically gives the twin thickness and twin volume fraction variations along the depth from the surface of the GNS layer. It shows that the average twin thickness is gradually decreased from ~130 nm at depth of ~ 80 μm to ~ 8 nm in the topmost surface. While, the corresponding twin volume fraction is slightly decreased from ~70% to 46%, maintaining the high-density deformation NTs in the GNT layer. As a result, our experimental results verify a high-performance GNT layer produced on CrCoNi MEA. Nonetheless, twinning mechanisms and their roles in the formation of the GNT layer should be further illustrated in the next section.

Deformation twinning has been known to be activated by nucleating and gliding Shockley partial dislocation on successive {111} planes in fcc metals. As shown in Fig. 2(c-e),

both parallel and intersecting deformation twinning can effectively refine the UFGs by segmenting them into smaller twin lamellae and/or rhombic blocks [24]. However, there is still limited literature to provide the atomic evidence to clarify the detailed refinement process for forming NGs, especially by twin-twin intersections. In addition to the rhombic blocks by segmenting, our atomic-scale observations dissect that NGs would be formed by grain rotating at the twin-twin intersecting region, thus leading to the grain refinement into the nanometer regime as indicated in the 20 μm-topmost surface layer. Fig. 3(a) shows a typical HRTEM image capturing the intersection behavior by two deformation NTs (i.e. Twin I and Twin II) growing along two {111} planes. A NG with grain size of ~ 25 nm is formed at the intersection region, which has a misorientation of ~ 10° with respect to Twin I around the same zone axis $[\bar{1}10]$, according to the corresponding diffraction patterns schematically summarized in Fig. 3(a). Fig. 3(b) and Fig. 3(c) give respectively atomic filtered images to dissect the atomic arrangement and crystalline defects in the interfacial regions between rotated grain (RG) and these two deformation NTs. On one hand, Fig. 3(b) directly shows that the $(\bar{1}\bar{1}\bar{1})_{RG}$ planes rotate with respect to $(\bar{1}\bar{1}\bar{1})_{TI}$ by ~10° around the zone axis $[\bar{1}10]$. Accordingly, a series of full dislocations with Burgers vector of $b_I = a/2[0\bar{1}1]$ are characterized to evenly distribute on almost every 6 (111) planes along the low-angle grain boundary (LAGB). The theoretical average spacing D = 12.52 Å along the [111] direction is anticipated from D = $b_{[11\bar{2}]}/\theta$, where $b_{[11\bar{2}]}$ denotes the component of the dislocations b_I and θ is the rotation angle. The interplanar spacing of every six (111) in our observations is 12.36 Å, which is in high alignment with the theoretical calculation. On the other hand, the symmetrical orientation relationship between the Twin II and Twin I in the intersection region (i.e. rotated NG region) is also changed, resulting in the decrease of the angle between $(\bar{1}\bar{1}\bar{1})_{TII}$ and $(\bar{1}\bar{1}\bar{1})_{TI}$ from original 141° to 131°. In this connection, a set of dislocations with Burgers vector of $b_{II} = a/2[\bar{1}01]$ are also characterized

to locate on every nine $(\bar{1}\bar{1}1)_{TII}$ planes, as shown in Fig. 3(c), which can theoretically induce a misorientation of ~6.8°. The rest of ~3.2° might be accommodated by atom shuffling and/or continuous lattice deformation in the interface [25, 26]. Besides, these dislocations could also release the misfit strain of 10% between $(00\bar{2})_{RG}$ and $(\bar{1}\bar{1}1)_{TII}$ planes.

It is interesting to note that the actions of "accumulation" and "spread out" can be reversibly triggered between a set of full dislocations on every certain number of planes and partials shearing on the successive planes, resulting in the typical interfacial structures during the phase transformation and/or grain rotations [25, 26]. In this study, two sets of full dislocations in the interfaces between two deformation NTs and rotated NG should be accumulated by the shearing of the twinning partials on every {111} plane for forming these two deformation NTs, as schematically shown in Fig. 3(d). Gliding any of three types of twinning partials (e.g. $\mathbf{b}_{p1} = a/6[\bar{1}\bar{1}2]$, $\mathbf{b}_{p2} = a/6[2\bar{1}\bar{1}]$, and $\mathbf{b}_{p3} = a/6[\bar{1}2\bar{1}]$ on the same (111) plane) can create the same deformation twins [27]. However, the components of these three partials along the $[\bar{1}10]$ direction are different, thus "accumulating" different full dislocations at GBs with different tilt angles. For example, when the twin is produced by twinning partials with the same burgers vector $\mathbf{b}_{p1}$ on successive {111} planes, the largest tilt angle of 35° can be achieved. While the smallest tilt angle of 0° could be generated if partials with three different burgers vector ($\mathbf{b}_{p1}$, $\mathbf{b}_{p2}$, and $\mathbf{b}_{p3}$) propagating in an equal number of times sequentially (i.e. $\mathbf{b}_{p1} + \mathbf{b}_{p2} + \mathbf{b}_{p3} = 0$), yielding zero macrostrain. In this regard, a tilt angle of ~10° in this study is induced by the accommodation of six twinning partials on six (111) planes, which is approximately closed to the integer combination of twinning partial as: $\mathbf{b}_{p1} : \mathbf{b}_{p2} : \mathbf{b}_{p3} = 2 : 2 : 1$. After passing through the rotated NG, these full dislocations continue to "spread out" a series of twinning partials for the Twin I. As for the Twin II, the twinning partials might have a combination of $\mathbf{b}_{p1} : \mathbf{b}_{p2} : \mathbf{b}_{p3} = 3 : 3 : 2$, i.e. a full dislocation is spread into eight twinning

partials on eight $(\bar{1}\,\bar{1}1)$ planes, close to every nine $(\bar{1}\,\bar{1}1)$ planes observed experimentally.

Twinning partials with zero-macrostrain combination might become predominant in refined NGs. Fig. 4 (a-e) shows the HRTEM images of two typical refined NGs in the 20 μm-topmost surface, which are embedded by two types of deformation NTs, i.e. parallel NTs in Fig. 4(a-b) and multifold NTs in Fig. 4(c-d), respectively. Both types of deformation NTs should be nucleated and grown via twinning partials from GBs. In particular, Fig. 4(b) gives the enlarged rectangle from Fig. 4(a), indexing a typical 9R phase structure along TB, which can be proven by the extra diffraction spots with three times interplanar spacing from the diffraction patterns inserted in Fig. 4(a). It has been reported that deformation twinning in NG metals can be accomplished via the migration of 9R phase interfacial structure by cooperative passage of a set of twinning partials with a repeatable sequence $\mathbf{b}_{p1}$:$\mathbf{b}_{p2}$:$\mathbf{b}_{p3}$ on every {111} plane, as indicated in Fig. 4(b), which yields a zero-net macrostrain [28]. 9R phase structures are also observed to assist the deformation multifold NTs, as the atomic-filtered image inserted in Fig. 4(c). In addition, high-density SFs can be found along the TBs, as shown in Fig. 4(d). Noticeably, there are smooth GB segments at locations intersecting the TBs in Fig. 4(c), as indicated by Fig. 4(e), which could also suggest the zero-macrostrain twinning mechanism. Accordingly, Fig. 4(f-i) depicts the simulated atomic-scale evolution of a representative deformation fivefold NT in one NG during the SPCBNT process. At the initial stage, several partials are found in Fig. 4(f) to nucleate and emit from GB. Three types of twinning partials ($\mathbf{b}_{p1}$, $\mathbf{b}_{p2}$, and $\mathbf{b}_{p3}$) can be indexed on three successive (111) planes, generating TB0 with a total $\mathbf{b}$ of zero. This could be a typical zero-macrostrain random activation of partials (RAP) twinning mechanism [27], which induces no deformation affecting the neighboring lattice structures, consistent with the experimental observations in Fig. 4(c). The RAP twinning partials are also verified to emit from GB for forming TB1 in the subsequent Fig. 4(g). A typical two multifold twin is formed with intersecting TB1 and TB2, as shown in Fig. 4(h). Finally,

twinning partials from GBs to complete the TB3, TB4, and TB5, as shown in Fig. 4(i), which are jointed to accomplish the fivefold NT in NG. As a result, our experimental and simulated results consistently reveal the zero-macrostrain multifold twinning mechanisms within refined NGs in the 20 μm-topmost surface layer.

SSPD approaches have been used to fabricate GNS metals with deformation twinning, such as steels [12], Cu-4.5 wt% Al alloys [29], and CrCoNi MEAs[16]. However, there is still limited work reporting the large-length scale GNT and underlying twinning mechanisms governing the gradient refinement process. In this study, a high-performance GNT layer with gradient distribution of deformation twins in both UFGs and NGs has been successfully produced on CrCoNi MEA alloy by high-strain rate SPCBNT technique, as schematically shown in Fig. 5. More specifically, our atomic evidence elucidates the size-dependent twinning mechanisms accomplishing the gradient refinement process, especially including the twin-twin intersections refinement with rotation of the intersected nanograins and zero-macrostrain deformation nanotwinning in refined nanograins. It should be noticed that these deformation twins in the GNT layer are all nucleated by twinning partials, which are activated by the sufficient stress provided high-strain rate SPCBNT process. On one hand, the shear stress required to trigger a twinning partial can be expressed as [30, 31]: $\tau_p = 2\alpha\mu b_p / D + \gamma_{SFE} / b_p$, where μ is shear modulus (87 GPa), $\boldsymbol{b_p}$ is the magnitude of the Burgers vector of twinning partial (0.1456 nm), γ_{SFE} is the SFE (22 ± 4 mJ/m^2), D is the grain size, respectively. Apparently, the shear stress required in the top surface is the highest, as corresponding deformation NTs in NGs having the smallest grain size of ~ 25 nm. Taking α for 1, the highest shear stress for twinning partials could be calculated as ~ 1.16 GPa, which is equivalent to a normal stress of ~ 2 GPa. On the other hand, the surface equivalent stress provided by the SPCBNT process can be empirically described by the Johnson–Cook model [32]: $\sigma = (A + B\varepsilon^n)(1 + C\ln(\dot{\varepsilon} / \dot{\varepsilon}_0))$, where A, B, C, and n are yield stress, hardening modulus, strain rate sensitivity coefficient, and

hardening coefficient, which are determined from the dataset as 431 MPa, 1480 MPa, 0.0134, and 0.66, respectively. $\dot{\varepsilon}_0$ is the reference strain rate (1 s^{-1}). ε and $\dot{\varepsilon}$ are strain and strain rate, respectively, expressed as: $\gamma = \lambda / \cos\alpha' + 1/\lambda\cos\alpha' - 2\tan\alpha'$, $\varepsilon = \gamma/\sqrt{3}$, and $\dot{\varepsilon} = d\varepsilon/dt = \varepsilon V/\Delta$ in the machining process [33, 34]. In our experiments, α' is tool rake angle ($-20°$), $\lambda = t_c/t_\mu$ (t_c and t_μ are chip thickness of 8 μm and cutting depth of 10 μm). V is the cutting speed (267 mm/s) and Δ is the thickness of the deformed zone (~ 150 μm). Accordingly, plastic strain of 1.68 and strain rate of 3.0×10^3 s^{-1} are obtained to estimate the equivalent stress of ~ 2.78 GPa in the top surface provided by SPCBNT process, which exceeds the normal stress required for twinning partial (~2 GPa). Consequently, the gradient stress distributed along the depth direction during the SPCBNT process could activate the gradient deformation twins for forming GNT layer.

SY and LQ were supported by the grants from the Research Committee of PolyU under student account codes RK2J and RK2U, respectively. XSY acknowledges the support from the National Natural Science Foundation of China (NSFC) Projects (Nos. 51701171 and 51971187), and funding support to the State Key Laboratories in Hong Kong from the Innovation and Technology Commission of the Government of the HKASR, China. XSY also acknowledges the support from the PolyU Research Office (No. 1-BBXA). BG acknowledges the support from the National Key R&D Program of China (2017YFA0700703) and NSFC Project (No. 92060102). HW acknowledges the NSFC projects (Nos. 51901013 and 52071023).

References:

[1] M.A. Meyers, A. Mishra, D.J. Benson, Prog. Mater. Sci. 51 (4) (2006) 427-556.
[2] J. Schiøtz, K.W. Jacobsen, Science 301 (5638) (2003) 1357-1359.
[3] S. Zheng, I.J. Beyerlein, J.S. Carpenter, K. Kang, J. Wang, W. Han, N.A. Mara, Nat. Commun. 4 (1) (2013) 1-8.
[4] K. Lu, L. Lu, S. Suresh, Science 324 (5925) (2009) 349-352.
[5] X. Wu, M. Yang, F. Yuan, L. Chen, Y. Zhu, Acta Mater. 112 (2016) 337-346.
[6] Z. Yin, X. Yang, X. Ma, J. Moering, J. Yang, Y. Gong, Y. Zhu, X. Zhu, Mater. Des. 105 (2016) 89-95.
[7] S. Wang, S. Wang, H.-H. Wu, Y. Wu, Z. Mi, X. Mao, Sci. Bull. (2021)
[8] J. Lu, K. Luo, Y. Zhang, G. Sun, Y. Gu, J. Zhou, X. Ren, X. Zhang, L. Zhang, K. Chen, Acta Mater. 58 (16) (2010) 5354-5362.
[9] S. Curtze, V.-T. Kuokkala, Acta Mater. 58 (15) (2010) 5129-5141.
[10] Z. Cheng, L. Lu, Scr. Mater. 164 (2019) 130-134.
[11] Z. Cheng, H. Zhou, Q. Lu, H. Gao, L. Lu, Science 362 (6414) (2018)
[12] Y. Wei, Y. Li, L. Zhu, Y. Liu, X. Lei, G. Wang, Y. Wu, Z. Mi, J. Liu, H. Wang, Nat. Commun. 5 (1) (2014) 1-8.
[13] Y. Ye, Q. Wang, J. Lu, C. Liu, Y. Yang, Mater. Today. 19 (6) (2016) 349-362.
[14] Z. Zhang, H. Sheng, Z. Wang, B. Gludovatz, Z. Zhang, E.P. George, Q. Yu, S.X. Mao, R.O. Ritchie, Nat. Commun. 8 (1) (2017) 1-8.
[15] G. Laplanche, A. Kostka, C. Reinhart, J. Hunfeld, G. Eggeler, E. George, Acta Mater. 128 (2017) 292-303.
[16] W. Guo, Z. Pei, X. Sang, J.D. Poplawsky, S. Bruschi, J. Qu, D. Raabe, H. Bei, Acta Mater. 170 (2019) 176-186.
[17] T.L. Brown, C. Saldana, T.G. Murthy, J.B. Mann, Y. Guo, L.F. Allard, A.H. King, W.D. Compton, K.P.

Trumble, S. Chandrasekar, Acta Mater. 57 (18) (2009) 5491-5500.
[18] S.S. To, H. Wang, W.B. Lee, Materials characterisation and mechanism of micro-cutting in ultra-precision diamond turning, Springer, 2018.
[19] H. Fu, X. Zhou, B. Wu, L. Qian, X.-S. Yang, J. Mater. Sci. Technol. (2021)
[20] B. Gan, J.M. Wheeler, Z. Bi, L. Liu, J. Zhang, H. Fu, J. Mater. Sci. Technol. 35 (6) (2019) 957-961.
[21] S. Plimpton, J. Comput. Phys. 117 (1) (1995) 1-19.
[22] D. Farkas, A. Caro, J. Mater. Res. 33 (19) (2018) 3218-3225.
[23] J. Tersoff, Phys. Rev. B. 37 (12) (1988) 6991.
[24] N. Tao, K. Lu, Scr. Mater. 60 (12) (2009) 1039-1043.
[25] X.-S. Yang, S. Sun, H.-H. Ruan, S.-Q. Shi, T.-Y. Zhang, Acta Mater. 136 (2017) 347-354.
[26] X.-S. Yang, S. Sun, T.-Y. Zhang, Acta Mater. 95 (2015) 264-273.
[27] Y. Zhu, X. Liao, X. Wu, Prog. Mater. Sci. 57 (1) (2012) 1-62.
[28] L. Liu, J. Wang, S. Gong, S. Mao, Phys. Rev. Lett. 106 (17) (2011) 175504.
[29] J. Wang, N. Tao, K. Lu, Acta Mater. 180 (2019) 231-242.
[30] K. Lagerlöf, J. Castaing, P. Pirouz, A. Heuer, Philos. Mag. 82 (15) (2002) 2841-2854.
[31] J.P. Hirth, J. Lothe, T. Mura, Theory of dislocations, second ed., American Society of Mechanical Engineers Digital Collection, 1983.
[32] Z. Pu, D. Umbrello, O. Dillon Jr, T. Lu, D. Puleo, I. Jawahir, J. Manuf. Process. 16 (2) (2014) 335-343.
[33] Y. Guo, C. Saldana, W.D. Compton, S. Chandrasekar, Acta Mater. 59 (11) (2011) 4538-4547.
[34] M. Efe, W. Moscoso, K.P. Trumble, W.D. Compton, S. Chandrasekar, Acta Mater. 60 (5) (2012) 2031-2042.
[35] B. Schuh, R. Pippan, A. Hohenwarter, Mater. Sci. Eng. A. 748 (2019) 379-385.
[36] P. Sathiyamoorthi, P. Asghari-Rad, J.W. Bae, H.S. Kim, Intermetallics 113 (2019) 106578.
[37] M. Yang, D. Yan, F. Yuan, P. Jiang, E. Ma, X. Wu, Proc. Natl. Acad. Sci. U.S.A. 115 (28) (2018) 7224-7229.
[38] C. Slone, J. Miao, E.P. George, M.J. Mills, Acta Mater. 165 (2019) 496-507.
[39] K. Jiang, B. Gan, J. Li, Q. Dou, T. Suo, Mater. Sci. Eng. A. (2021) 141298.
[40] Y. Liu, Y. He, S. Cai, J. Alloys Compd. 853 (2021) 157388.
[41] Y. Liu, Y. He, S. Cai, Mater. Sci. Eng. A. 801 (2021) 140429.
[42] R. Wen, C. You, L. Zeng, H. Wang, X. Zhang, J. Mater. Sci. 55 (2020) 12544-12553.
[43] B. Schuh, B. Völker, J. Todt, K.S. Kormout, N. Schell, A. Hohenwarter, Materials 11 (5) (2018) 662.

Figure 1

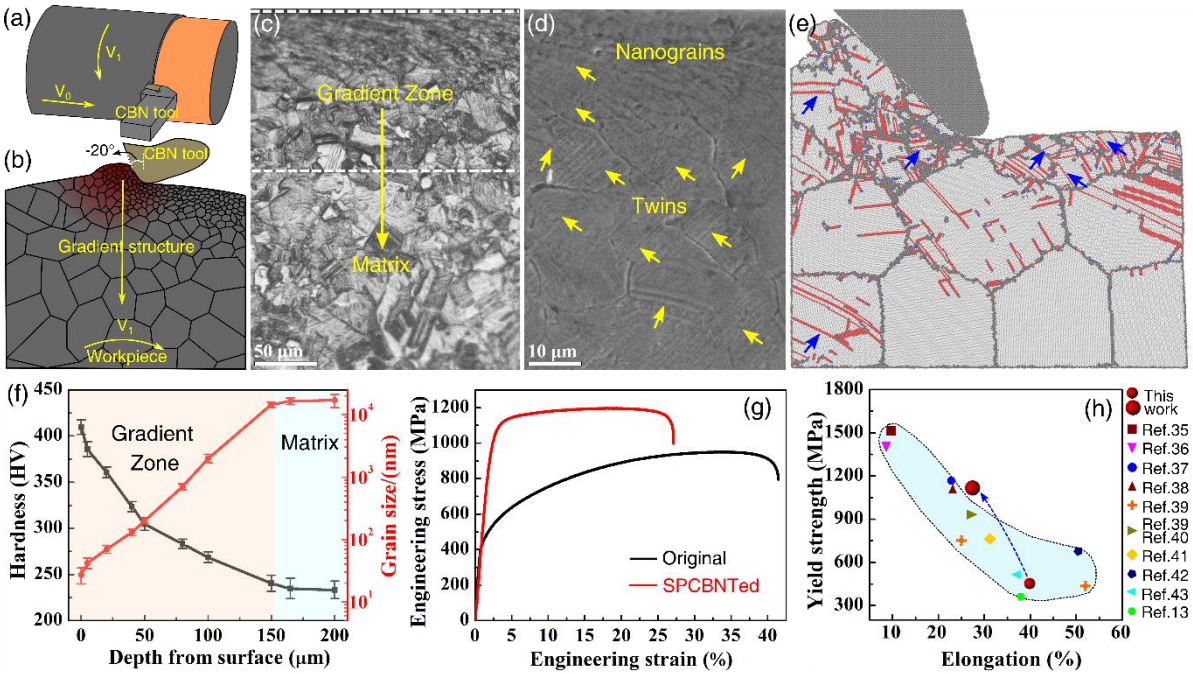

Figure 1. SPCBNT-fabricated GNS CrCoNi MEA with strength-ductility synergy. (a) Schematic diagrams of the SPCBNT process. (b-c) Cross-sectional OM and SEM images showing the SPCBNT-induced gradient structure. (e) MD simulation of SPCBNT process. (f) Hardness and grain size variation of the produced GNT CrCoNi MEA along the depth direction from the surface to matrix. (g) Engineering stress-strain curves of original and SPCBNTed specimens. (h) Summarized yield strength versus total elongation plot of CrCoNi MEAs at room temperature.

Figure 2

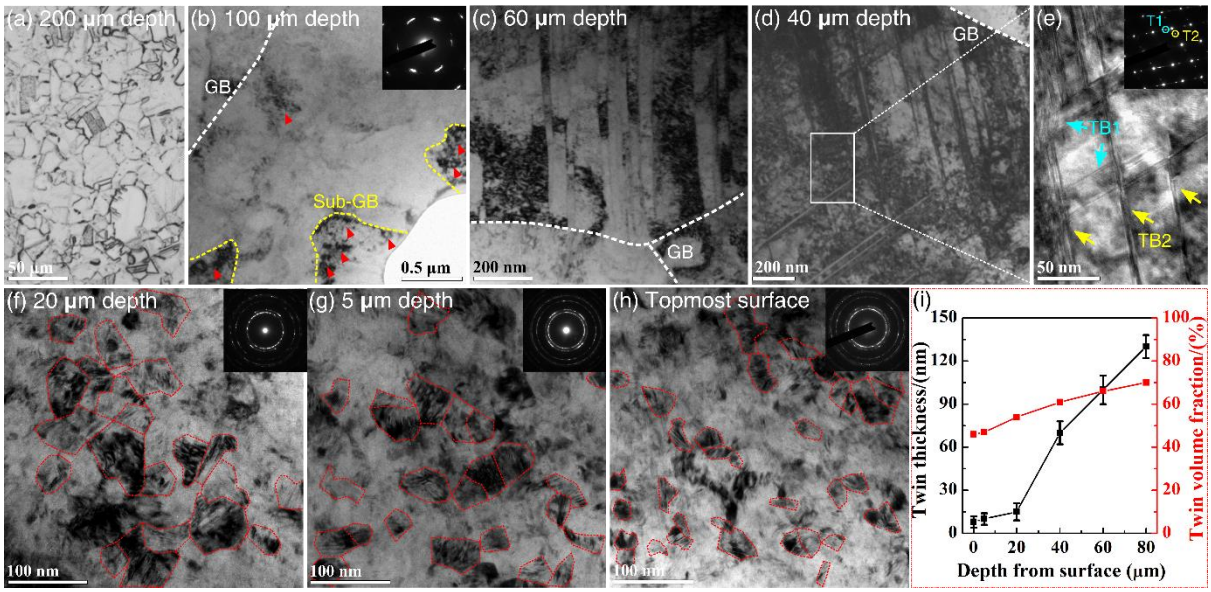

Figure 2. Microstructural evolution of GNT CrCoNi MEA. (a) OM image at depth of ~200 μm (matrix). (b-h) A series of typical TEM images at different depths from (b) ~ 100 μm, (c) ~ 60 μm, (d-e) ~ 40 μm, (f) ~ 20 μm, (g) ~ 5 μm, to (h) 0 μm (topmost surface) showing the formation of GNT CrCoNi MEA. (i) Statistical curves of twin thickness and twin volume fraction dependences on the depth from the surface.

Figure 3

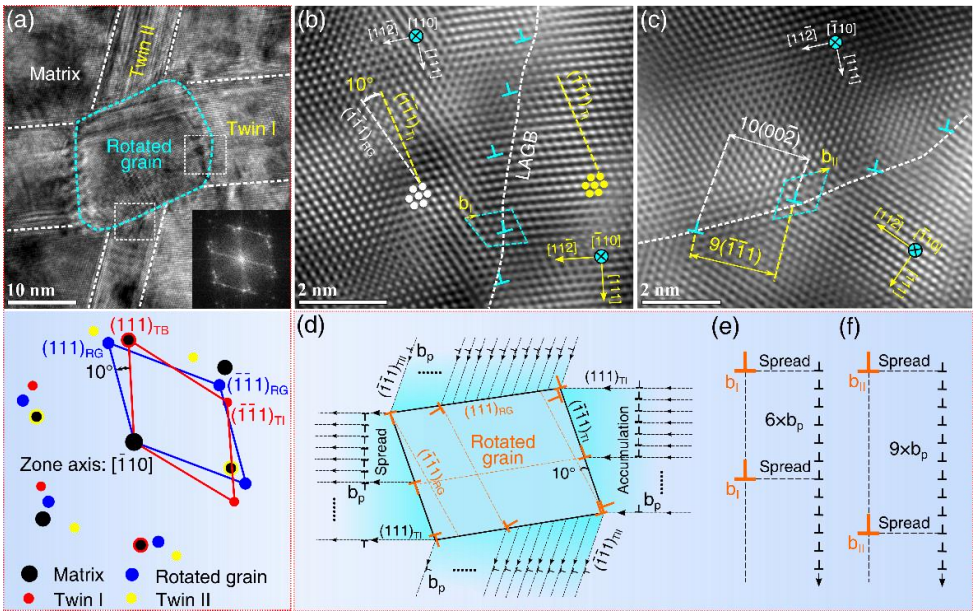

Figure 3. Grain refinement induced by the twin-twin intersections in the GNT CrCoNi MEA. (a) A typical HRTEM image of the twin-twin intersection at a depth of ~40 μm, and schematically summarized diffraction pattern showing the NG with a grain rotation of ~10° in the intersected region. (b-c) Atomic-filtered images of the rectangle regions in (a). (d-f) Schematic illustration of the grain rotation of ~10° induced by the intersection of two deformation twinning, and (e-f) the actions of "accumulation" and "spread" between twinning partials and full dislocations.

Figure 4

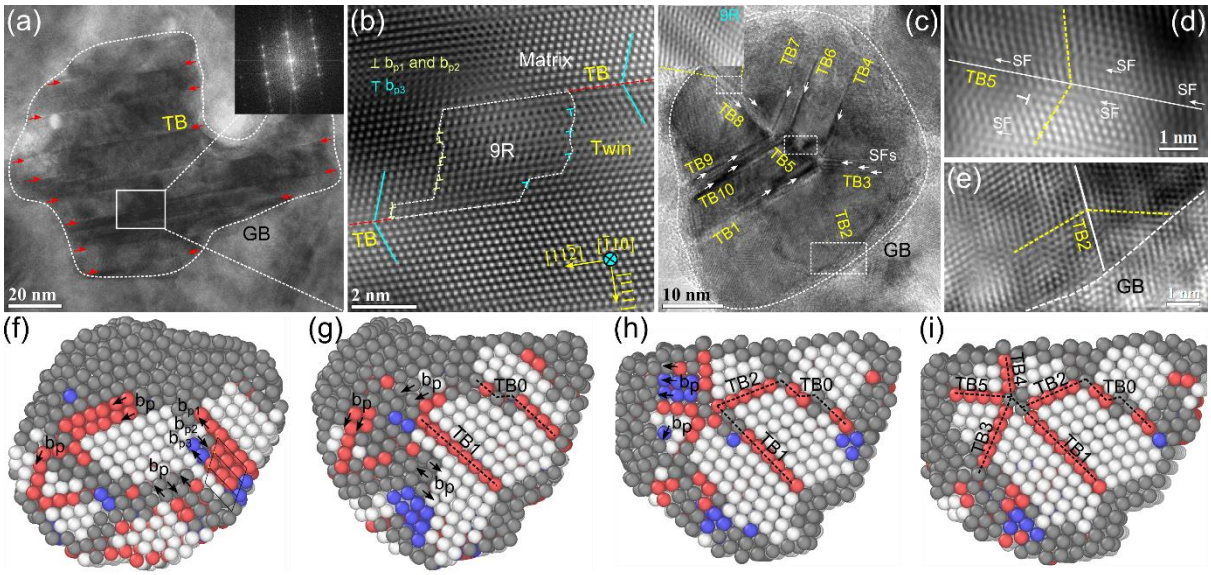

Figure 4. Zero-macrostrain deformation nanotwinning in the refined NGs. (a) A typical HRTEM image in the 20 µm-topmost surface showing the deformation parallel NTs in NG. (b) Atomic-filtered image enlarged from rectangle in (a) showing the 9R phase structure along TBs. (c) A typical HRTEM image in the 20 µm-topmost surface showing the deformation multifold NTs in NG. (d-e) Atomic-filtered image enlarged from rectangles in (c) showing the high-density SFs along the TBs and smooth GB segments at locations intersecting the TBs. (f-g) Atomistic simulation of a typical deformation fivefold NT in NG, showing the twinning process of TB0, TB1, TB2, TB3, TB4, and TB5 via twinning partials (i.e. RAP) from GBs for the formation of the fivefold NT in NG. *(Atoms are coloured using the common neighbour analysis (CNA), white for FCC atoms, red for HCP atoms, blue for BCC atoms and grey for other atoms.)*.

Figure 5

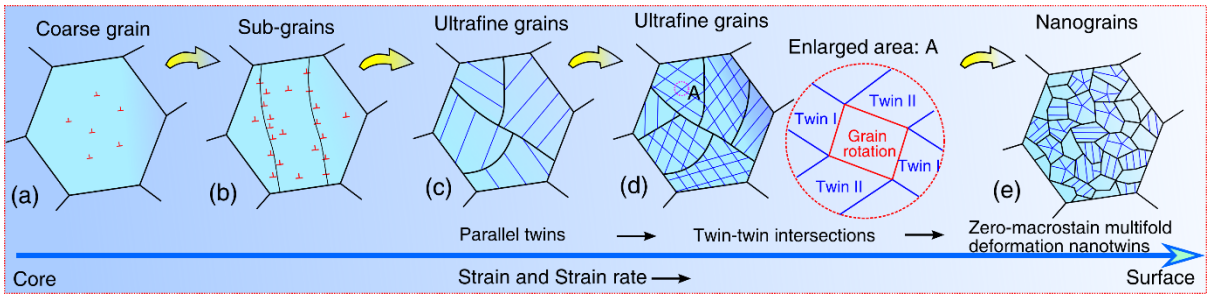

Figure 5. Schematic diagram of the gradient refinement process. It includes (a) coarse grains, (b) sub-grains, (c) parallel twins refining UFGs, (d) twin-twin intersections refining rhombic blocks and rotating the intersected NGs in UFGs, and (e) zero-macrostrain deformation nanotwinning in the refined NGs along the gradient depth direction.